ARTICLE OPEN

Rapid prediction of cementitious initial sorptivity via surface wettability

Hossein Kabir[1] and Nishant Garg[1]✉

The tendency of cementitious systems to absorb and transmit liquid through capillary pores is often characterized by initial sorptivity, which is an important indicator of long-term durability. However, sorptivity measurements, which are based on the continuous mass change of specimens exposed to water, are labor-intensive (up to 6 h of continuous measurements). Here, we exploit the fundamental surface-wetting characteristics of cementitious systems to estimate their sorptivity in a rapid fashion, i.e., in a matter of few minutes. In a series of 63 distinct paste systems of varying w/c ratios (0.4–0.8), subject to a range of curing periods (1–7d), we establish strong correlations (adjusted $R^2 \geq 0.9$) between the initial sorptivity (~6 h) and dynamics of drop spreading (contact angle ~0.5 s, drop residence time <10 min). These results elucidate rapid pathways in estimating initial sorptivity and durability of a broad variety of hydrated cementitious matrices.

npj Materials Degradation (2023)7:52 ; https://doi.org/10.1038/s41529-023-00371-4

INTRODUCTION

Every year, more than 4 billion tons of cement is produced worldwide as the fundamental building block of industrialized society, and this number is expected to grow until 2050 due to urbanization and population growth[1]. As cement and concrete infrastructure undergoes aging and degradation, long-term durability of cementitious materials becomes increasingly important. Durability issues such as chloride-induced corrosion have become one of the largest challenges to the reliability and safety of our built infrastructure[2]. The durability of cementitious systems largely depends on the penetration of fluids and ionic species, known as transport properties, which are mainly influenced by the pore system[3]. There are three main mechanisms that have been reported to govern the transport properties of cementitious systems: absorption[4], diffusion[5], and permeability[6], all impacted by the volume fraction and connectivity of pores. In particular, *absorption* is the ability of a cementitious matrix to take in water using the capillary suction mechanism, *diffusion* is the ion movement triggered by the concentration gradient in a cementitious system, and *permeability* estimates the liquid flow under an applied hydraulic pressure gradient throughout a matrix[7]. To determine the transport properties of cementitious systems, a number of standard test procedures currently exist, which include rapid chloride permeability[8], surface resistivity[9], chloride ponding[10], bulk diffusion[11], non-steady-state chloride migration[12], penetration of water under pressure[13], and water absorption[14].

Among these procedures, water absorption tests are commonly used for assessing the durability of cementitious systems[15]. This water absorption test is typically done in accordance with ASTM C1585[14] to determine the rate of absorption (*sorptivity*) of water by unsaturated cementitious systems, which is related to its hydraulic diffusivity[16]. In this experiment, the process of water absorption is divided into *initial* (rapid) and *secondary* (steady) sorptivity stages. In particular, for unsaturated specimens, the initial stage of water absorption is controlled by *capillary absorption*, which is influenced by the volume fraction and distribution of the capillary pores, and dictates the durability of cementitious systems. While the secondary stage corresponds to the *total porosity* of the matrix, which impacts the moisture diffusion through gel pores, it fails to provide sufficient information on durability[17–20]. Subsequently, pinpointing the *initial* sorptivity of cementitious materials often takes the center stage in estimating their long-term performance. However, this commonly used sorptivity test is both labor-intensive and time-consuming. Specifically, it requires the operator to continuously measure and re-measure the weight of the specimen several times for up to 6 h. To make this experiment less laborious, automated techniques have been proposed in the literature[7,21]. However, these automated techniques still require several hours of operation. Hence, there is a need to develop an automated test, which can also reduce the *time* associated with sorptivity measurements.

To address this issue of time, we are proposing a rapid characterization method based on surface wettability which can result in reliable estimation of initial sorptivity in cementitious systems. Surface wettability, which entails the dynamics of drop spreading is a fundamental material property[22]. On porous substrates, in general, the dynamics of drop spreading are governed by four main mechanisms: viscous forces, surface tension, capillary forces, and gravitational forces[23], in which the last effect can be neglected for relatively small drops[24]. Essentially, the drop spreading on porous substrates can be studied by contact angle (CA) measurements[25]. CA is the tangent angle created by the drop on a solid surface at the ternary phase (i.e., gas-liquid-solid) contact point for characterizing wettability. The CA represents the macroscopic behavior of liquids and is controlled by both the *drop surface tension*, i.e., a cohesion force that limits spreading, and the *solid surface energy*, i.e., an adhesion force that promotes spreading[26]. Broadly speaking, on nonwetting or hydrophobic surfaces, the CAs are larger than 90°, while hydrophilic surfaces have CAs smaller than 90°[27]. These wettability characteristics have been commercially exploited to create a variety of materials and coatings with desirable properties such as anti-corrosion and self-cleaning[28–30]. Finally, and more importantly, for a variety of materials such as natural stone, and paper species of varying porosities and permeabilities, water absorption

[1]Department of Civil and Environmental Engineering, University of Illinois Urbana-Champaign, Urbana, IL, US. ✉email: nishantg@illinois.edu

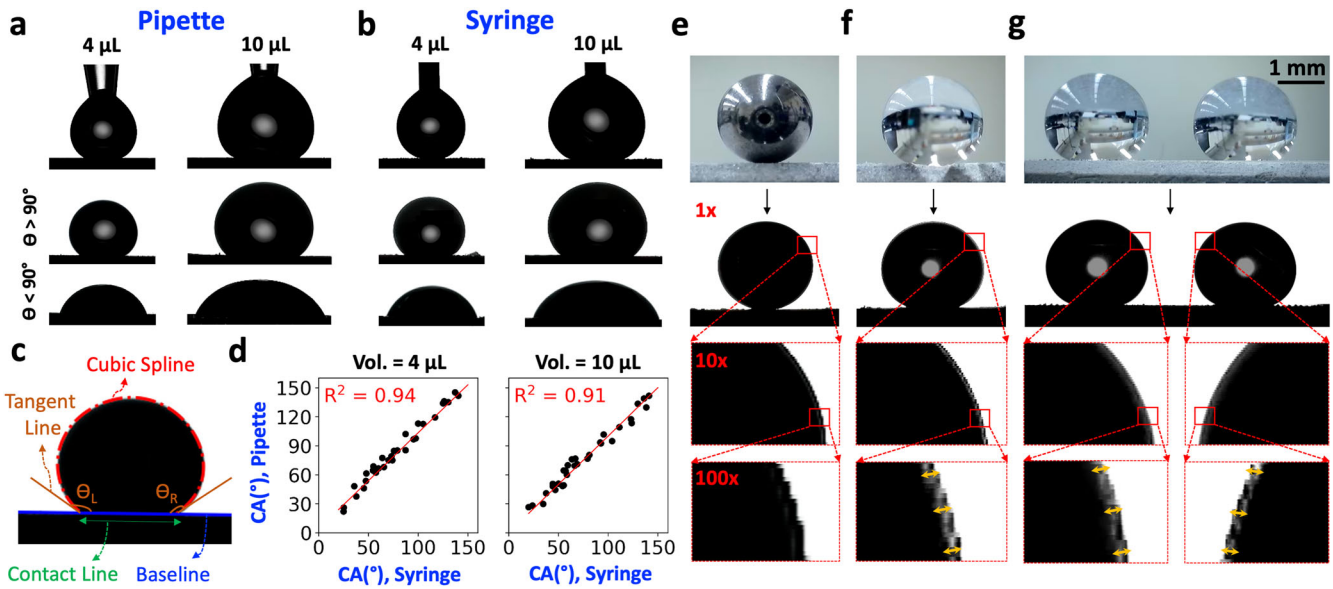

Fig. 1 Impact of the liquid dispensing system on the tangent angles at the ternary phase contact point. a Pipette tip dispensing 4 ± 0.2 µL or 10 ± 0.2 µL of deionized water drop on paste substrates, **b** syringe needle dispensing 4 ± 0.2 µL or 10 ± 0.2 µL of deionized water drop on paste substrates, **c** leveraging cubic spline polynomial fitting to determine the tangent angles (θ) at the ternary phase contact point, note that the bright spot (located in the middle of the back-lit drop) is manually removed, **d** matching the CAs of different drop volumes dispensed by pipette and syringe on substrates of varying wettability, estimating the ambiguity of pixel (grayscale) values at the circular boundary of (**e**) a single back-lit steel ball, (**f**) a single back-lit liquid drop, and (**g**) a pair of back-lit liquid drops. Therefore, the CA is primarily determined by the properties of the liquid and the surface, not the type of liquid dispenser or the drop volume (as long as it varies from 4 to 10 µL). However, the rate of liquid dispensed can affect wetting behavior.

has shown to be strongly correlated with their wettability characteristics[31,32].

Thus, in this study, we intend to explore and determine whether any meaningful correlation can be established between the surface wettability and sorptivity of *cementitious* systems. For this reason, three different ASTM Type 1 cements were cast at 5 different water-to-cement (w/c) ratios of 0.4, 0.5, 0.6, 0.7, and 0.8, and moist cured for 1, 3, and 7 days. The paste specimens were then subjected to water absorption tests in accordance with the ASTM C1585 to mark their initial sorptivity. In parallel to the standard ASTM C1585 sorptivity tests, the static and dynamic CA measurements were done on the surface of paste specimens by dispensing a controlled 4 ± 0.2 µL of deionized water droplets. Interestingly, these experiments revealed the existence of strong correlations (adjusted $R^2 \geq 0.9$) between the initial sorptivity (as determined by ASTM C1585 over several hours) and the fundamental wetting properties (e.g., initial CA, CA decrease rate, square root of drop residence time, initial drop volume, and drop volume decrease rate) obtained by our rapid contact angle goniometry setup in a matter of a few seconds to a few minutes.

RESULTS AND DISCUSSION

Impact of water dispensing system

The accuracy of CA measurements is not only affected by the shape and volume of drops but also by the fitting algorithm leveraged to determine the drop profile[33]. To exclude the effect of gravity, the drop diameter should not exceed the capillary length (λ) of 2.73 mm for deionized water, which is estimated by the following equation[34]:

$$\lambda = \sqrt{\frac{\gamma}{\rho g}} \tag{1}$$

where ρ is liquid density (i.e., 997 kg.m^{-3} for deionized water), g is gravity (9.81 m.s^{-2}), and γ is surface tension (calculated to be around 71.99 mN·m^{-1} for deionized water, see the methods section). Therefore, the maximum volume of deionized water (at 23 °C and 50% RH) should not exceed 10.65 µL such that the drop geometry would not be significantly deformed by its own weight. On the other hand, drops smaller than 3 µL should not be analyzed as they are easily disturbed by the liquid dispensing system and their prolonged kinetic energy dissipation. In addition, sub-microliter drops, i.e., nano- and pico-liter, can evaporate in seconds (or milliseconds) and need to be analyzed using expensive high-frame-rate (100–2000 fps) cameras. Therefore, to ensure statistical validity, we dispensed 4 ± 0.2 µL and 10 ± 0.2 µL of deionized water drops on the surfaces of paste cubes using a syringe needle or a pipette tip to determine how the liquid volume and type of dispenser would impact the results (see Fig. 1). Considering Fig. 1a, b, it is realized that regardless of the type of dispenser and liquid volume, the overall geometry of as-placed drops (measured at 0.5 s) does not change significantly. The fixed diameter of the dispensers is used as an internal reference for calibrating the length measurements against the variations in the optical distance or focal length of the camera.

For precise CA estimations, the cubic spline polynomials (Fig. 1c) are fitted on $N \geq 6$ points on the drop boundary with a numerical step size of $\Delta h \leq 0.05$, based on the parameter optimization results reported in Supplementary Fig. 1a. It is worth noting that the cubic spline and drop snake (ImageJ plugin)[35] algorithms provide comparable CA measurements; however, the former technique is easier to implement. In other words, as illustrated in Supplementary Fig. 1b, the experience of the user has less impact on the accuracy of cubic spline-based CA measurements as this technique has fewer parameters to adjust compared to the drop snake method. Followed by optimizing the parameters of the cubic spline fitting algorithm for accurate tangent line estimations (Supplementary Fig. 1a), the dispensed drops are shown to have similar initial CAs (at 0.5 s) on surfaces of varying wettability, i.e., ranging from 20 to 150°, regardless of their dispensed volume (Fig. 1d). In addition, as opposed to the back-lit image of an ideal steel ball (that has a sharp grayscale transition between the dark and bright regions, see Fig. 1e), there are 3–4

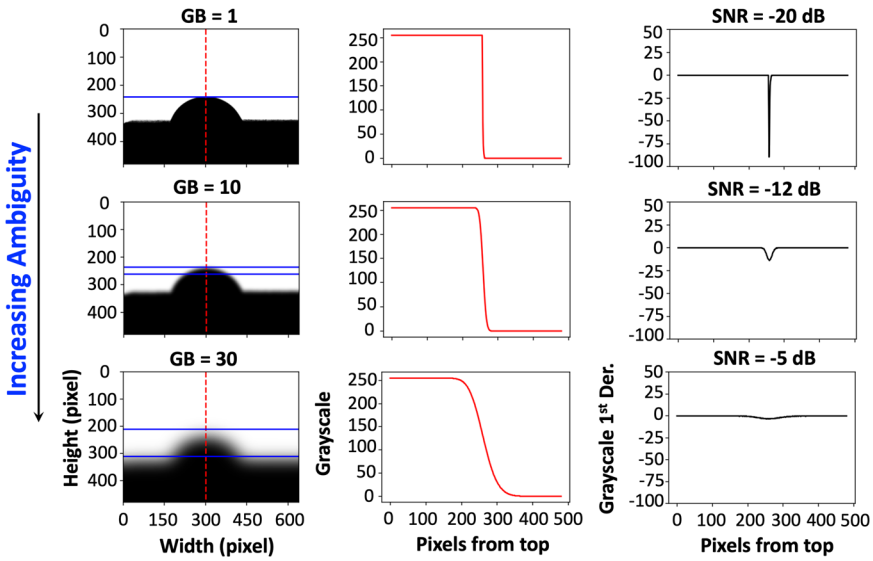

Fig. 2 Assessing the accuracy of CA measurements by estimating the SNR at the drop boundaries. left column: selecting a grayscale hydrophilic drop image and collecting the pixel values situated along the red dashed line, middle column: plotting the grayscale value of the pixels along the red dashed line, right column: estimating the 1st derivative of the grayscale values, calculating the SNR, and repeating the whole process for images synthetically blurred at GB = 1 (top row), GB = 10 (middle row), GB = 30 (bottom row). In addition, Supplementary Appendix 1 provides the Python code for measuring the SNR of each drop image.

ambiguous pixels at the liquid drop boundary (marked with double-headed orange arrows in Fig. 1f), which are unavoidable (in the absence of objective lens) and may result in a subtle optical error. Moreover, simultaneous analysis of more than one drop would not amplify the ambiguity at the boundaries proving that the extent of systematic error remains unchanged (Fig. 1g). It should be noted that errors in surface wettability measurements can be caused by both humans and devices. Supplementary Fig. 2a confirms that inexperienced users may incorrectly mark the ROI, leading to significant errors, i.e., more than 5 degrees. However, as long as the resolution is around 10 μm.pixel^{-1}, the choice of camera does not greatly affect the reliability of wettability assessments, hence the ambiguity at the drop boundary is not an issue (Supplementary Fig. 2b).

It has been shown that uncertainties in localizing the drop profile can lead to a substantial error in the estimated CA[36]. Therefore, the ability to analyze perfectly focused hydrophilic or hydrophobic drop images is a must for accurate wettability measurements. To determine whether the captured images are focused, the grayscale luminance of pixels (varying from 0 to 255) was stored along with the height of the hydrophilic drop image, i.e., the red dashed line in the leftmost column of Fig. 2. This grayscale pixel luminance is plotted as a function of the number of pixels from the top of the image in the mid-column of Fig. 2. Then, the first derivative of the pixel grayscale values is calculated to estimate the SNR of each image and then plotted in the rightmost column of Fig. 2. Furthermore, the Supplementary Appendix 1 includes the Python code utilized for quantifying the SNR of individual drop images. To simulate the analysis of unfocused images, the Gaussian Blurring (GB) filter, i.e., a programming library in Open CV[37], was used to synthetically convolute and blur the drop images. Synthetic convolution here refers to a matrix that transforms an image by applying a low-pass kernel over each pixel across the entire image to remove the details or high-frequency features. Basically, for GB = 1, the image remains unconvoluted and focused, while the edges of the drops are softened by increasing GB values. Subsequently, if the GB value of drop images increases from 1 to 30 (corresponding to the first and last row of Fig. 2, respectively), a dramatic reduction in the absolute SNR occurs (from 20 to 5 dB). In addition, as shown in the left column of Fig. 2, the uncertainties associated with the drop profile selection are marked with solid blue horizontal lines where the gap between the referred lines increases with a decrease in the absolute SNR values. Similar analyses are performed on hydrophobic drop images that have a bright spot in the middle and the absolute SNR value is found to exceed 20 dB for the focused image (see Supplementary Fig. 3 and Video 1). In particular, as shown in Supplementary Fig. 3 (middle column), the pixel values initially change from 255 (bright) to 0 (dark) at the outer drop boundary along the red dashed line. This process, i.e., the change in the pixel value, is reversed two more times at the inner drop boundaries showing that the changes in the pixel values (at the boundaries) are dramatic for a focused image, which results in a large (absolute) SNR value, i.e., >20 dB.

Moving further, to determine the impact of dispensed drop volume on the accuracy of CA measurements, the *dynamic* spreading of 4 ± 0.2 μL (Supplementary Fig. 4a) and 10 ± 0.2 μL (Supplementary Fig. 4b) drops are analyzed. These results in Supplementary Fig. 4b show that the changes in the focal length of the camera amplify for larger (10 ± 0.2 μL) moving/ absorbing drops. Supplementary Fig. 4c demonstrates the higher reduction in the absolute SNR of larger drops with time (from 21 to 14 dB in 30 s) when compared to the smaller drops (from 21 to 18 dB in 30 s). In summary, although drops of varying volumes have almost similar *initial* or *as-placed* CA at 0.5 s (Fig. 1d), smaller drops (i.e., 4 ± 0.2 μL) do seem to provide more accurate *dynamic* wettability measurements. The dispenser type, i.e., syringe or pipette, does not change the initial or dynamic CAs of absorbing drops. Consequently, in this study, smaller (4 ± 0.2 μL) drops are dispensed either by syringe or pipette for a more accurate wettability assessment of cementitious substrates. Supplementary Fig. 5 also confirms from Raman imaging, that a square area measuring 500 μm by 500 μm represents an appropriate size capable of fully capturing the surface heterogeneity. This indicates that 4 μL drops (with a radius of ~1 mm) can be reliably used to characterize the surface of cement paste specimens.

Impact of surface roughness

Apart from drop volume, surface roughness can significantly impact surface wettability results by amplifying both liquid repellence and wetting[38]. In particular, as long as the roughness

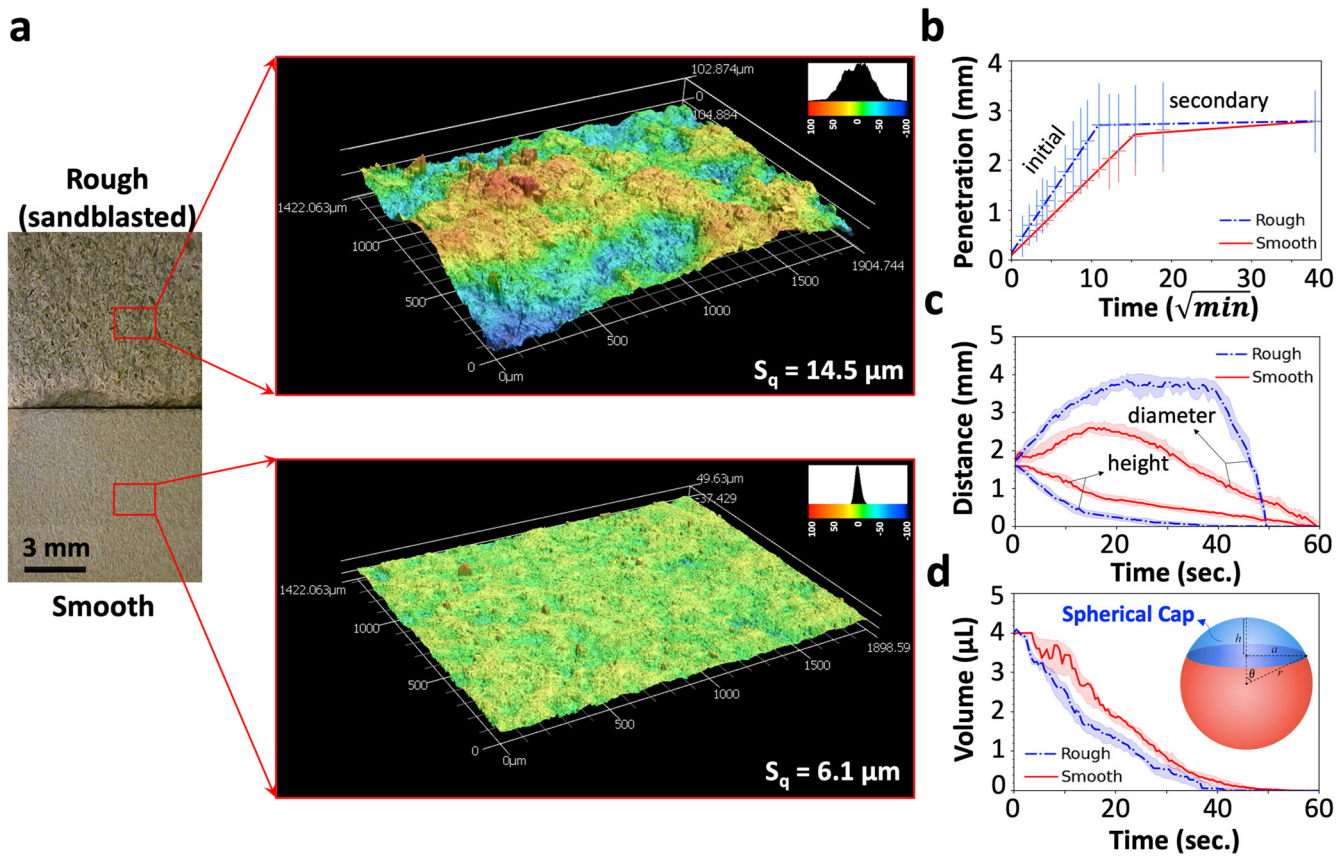

Fig. 3 Impact of surface roughness on initial sorptivity and dynamics of drop spreading. a Characterizing the roughness of smooth and sandblasted paste substrates made with Cem. A, w/c ratio of 0.5, and moist curing period of 7 days, **b** measuring the initial and secondary sorptivity of smooth and sandblasted specimens in accordance with the ASTM C1585, **c** finding the changes in the height and contact diameter of drops being absorbed on smooth and sandblasted surfaces, and (**d**) measuring the changes in the total volume of the drops using the spherical cap approximation, i.e., Eq. 2. It should be noted that uncertainties in the length and volume measurements are the range (max-min) of six measurements at each time point marked by shading regions around the average measurements.

is considerably smaller than the drop size, an increase in roughness can amplify wettability if the CAs are originally smaller than 90°, or it can alternatively increase liquid repellence if the CAs are initially larger than 90°[27,39]. For this reason, Supplementary Fig. 6 shows the procedure that is leveraged to accurately and unbiasedly measure the surface roughness of paste specimens. As shown in Supplementary Fig. 6a, for a specific ROI of 2100 µm by 2500 µm, the magnification is changed from 5 to 50× denoting that for both smooth and rough substrates the roughness values reached a plateau at 20× magnification, and a further increase in magnification would not significantly change the roughness results (Supplementary Fig. 6c). At 20× magnification, the area of analysis is changed from 1 to 36 blocks proving that regardless of surface topography (i.e., smooth or rough), at least 9 blocks are required for precise estimation of roughness (Supplementary Fig. 6d). Therefore, for statistical relevance and to precisely estimate the surface roughness of paste specimens using a laser profilometer, 9 blocks were analyzed at 20× magnification (see Supplementary Fig. 6b). It is also worth noting that since the maximum height of surface topographical inhomogeneity, (15 and 100 µm for smooth and sandblasted surfaces, respectively) is ~100× smaller than the drop contact line (1–4 mm), a substantial distortion in the drop profile, or optical error in registering the contact line, is less likely to occur[40,41]. Therefore, followed by pinpointing the surface roughness of paste specimens, it is of great importance to determine how the dynamics of drop spreading would be subject to change due to surface roughness.

The dynamics of drop spreading on porous substrates are mainly controlled by the combination of roughness filling and bulk penetration[42]. Figure 3a shows a smooth and rough (sandblasted for 2 s) specimen to further generalize the findings of this study against the variations in the surface roughness. Considering Fig. 3b, it is realized that the initial sorptivity (measured by the ASTM C1585) is higher for the sandblasted specimen, and the variation in the initial rate of absorption amplifies with an increase in surface roughness[43], whereas the total absorption remains unchanged. In addition, Fig. 3c shows that regardless of surface roughness, the contact diameter increases and then decreases with time[44]; however, on the rougher (sandblasted) surface, the drop spreads at a faster rate and then shrinks faster compared to the smoother surface (Fig. 3c). Assuming that the drop profile is axisymmetric and is part of a spherical cap, the liquid volume (V) and the tangent angle (θ) at the ternary phase contact point are estimated as follows[45]:

$$V = \frac{1}{6}\pi h\left[3a^2 + h^2\right] \approx \frac{1}{6}\pi h\left[3\left(\frac{d}{2}\right)^2 + h^2\right] \quad (2)$$

$$\theta = 2\tan^{-1}\left(\frac{h}{a}\right) \quad (3)$$

where h is the height of the drop, and a is the contact radius, which is approximately one-half of the contact line d (see Figs. 1c and 3d). Supplementary Fig. 7 showcases two absorbing drops, confirming that the drops are axisymmetric by matching the CAs estimated by direct (cubic spline fitting) and indirect

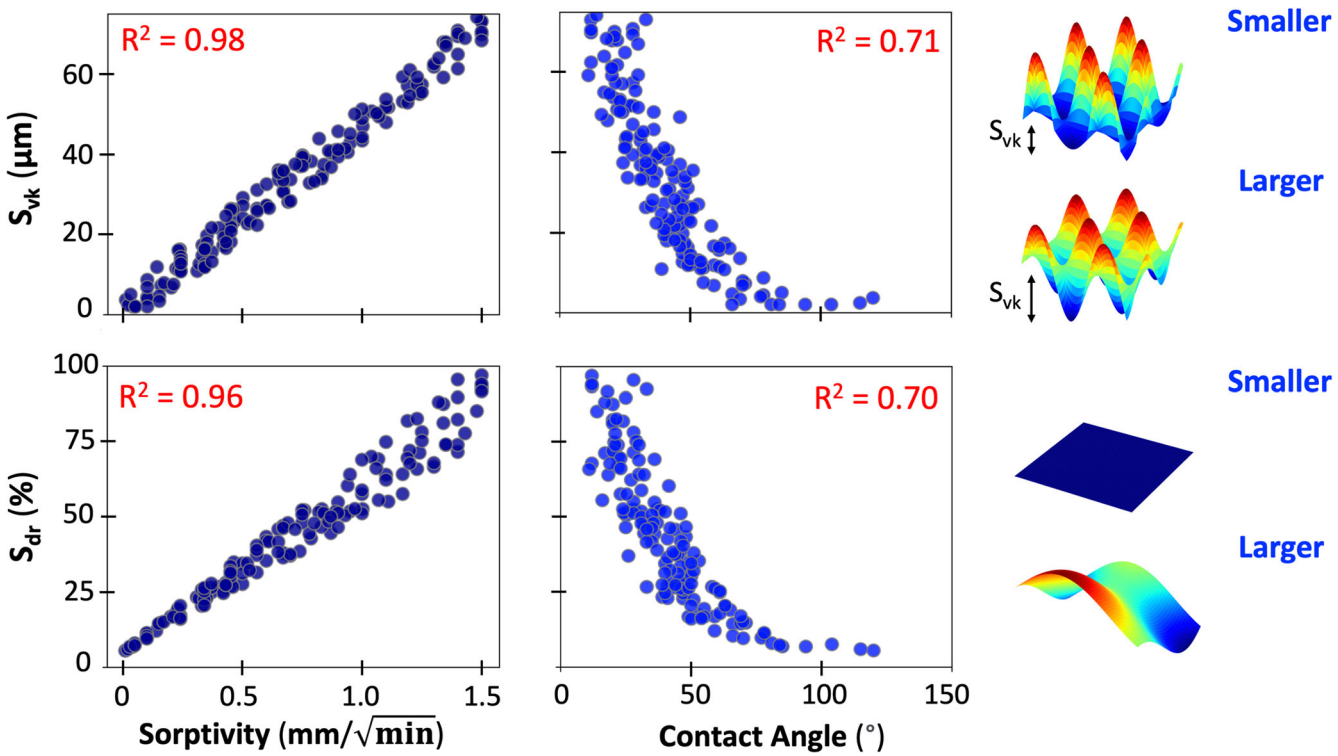

Fig. 4 Primary roughness indices that impact sorptivity and subsequently the wettability of cement pastes. This figure introduces two 'primary' roughness parameters, i.e., S_{vk} (average mean of valley depth), and S_{dr} (average developed interfacial area ratio) that are well correlated with sorptivity and wettability (i.e., CA) of cement pastes. In particular, the left column establishes the correlations between roughness parameters and sorptivity values, the middle column establishes the correlations between roughness parameters and CA values, and the right column schematically shows how the change in the roughness parameters would impact the surface of cement pastes. A surface with higher S_{vk} or S_{dr} values will have more surface area available for liquid absorption (increases sorptivity); therefore, the liquid has less time to form droplets or beads on the surface, and instead quickly wets the surface (decreases CAs).

(Eq. 3) methods for broad tangent angles, i.e., 15°–105°. As a result, Fig. 3d shows that the change in the drop volume versus time can be precisely estimated by Eq. 2. Considering this figure, the drop volume starts at 4 µL and constantly reduces with time due to the combination of bulk penetration (pore filling) and roughness spreading (film flow)[46,47]. Specifically, for the rougher (sandblasted) surface, the liquid imbibition is faster compared to the smoother surface (Fig. 3d), which confirms the higher sorptivity of drops on rougher surfaces (Fig. 3b). Subsequently, there exists a correlation between the initial rate of water absorption and the residence of drops on the paste surface, which is further detailed in the next section. Drop spreading is not affected by the surface tension of liquids if ranging from 50 to 73 ($mN{\cdot}m^{-1}$), implying that the choice of deionized water with a calculated surface tension of 71.99 $mN{\cdot}m^{-1}$ has a minor impact on the film flow[48,49]. Moreover, although the ASTM C1585 does not specify water quality for sorptivity measurements, liquid quality can impact the CA measurements. Particularly, potable water with ions (e.g., Na^{+}, Cl^{-}, and Ca^{2+}) can potentially affect surface-wetting behavior and subsequently, the CA values. Therefore, deionized water is recommended for more reliable estimates, as shown in Supplementary Fig. 8, with limited variations in results compared to potable water.

Surface wettability and sorptivity

Followed by pinpointing the overall impact of surface roughness on sorptivity and water repellence, this section determines whether liquid ingress into cementitious systems, i.e., absorption parameters, can be accurately estimated by analyzing the dynamics of drop spreading. Considering Supplementary Figs. 9 and 10, it is confirmed that for different mixtures, the initial sorptivity values lack a significant numerical range[6], denoting that a factor of 10 can fully cover the absorption range of various systems. The cumulative water absorption (penetration) increases with the square root of elapsed time ($t^{1/2}$) and shows a good linear fit due to four main reasons[50,51]: (1) the liquid flow in the cubic specimens (with 5 sealed sides) is approximately one-dimensional, (2) the cementitious systems are homogeneous, which supports the uniformity of mixing, casting, and curing, (3) the matrix is structurally unaltered during the short period of testing (≤24 h), and (4) the drying procedure (or conditioning) of 10 mm cubic specimens is uniform leading to similar initial water content. Furthermore, the sorptivity of various cementitious systems is reproducibly measured and varies in a rational way with curing history and composition. Specifically, Supplementary Fig. 11a shows the initial sorptivity of *smooth* cubic specimens (that are not sandblasted) made with Cements A to C, w/c ratios of 0.4 to 0.8, and a moist curing period of 1 to 7 days. Considering this subplot, a decrease in the w/c ratio or an increase in the moist curing period would densify the paste microstructure and limit the ingress of water through capillary pores due to the reduction in size and connectivity of the pore network.

Moreover, Supplementary Figs. 12 (1-day cured cement pastes), 13 (7-day cured cement pastes), and 14 (1–7-day cured silica-fume pastes) suggest that regardless of w/c ratios and chemical composition, the surfaces of 7-day cured specimens have smaller average heights than 1-day cured specimens, which is inferred from the skewness of height distribution subplots. However, due to the presence of precipitated $Ca(OH)_2$ inhomogeneities on the surfaces of 7-day cured specimens (after long-term exposure to

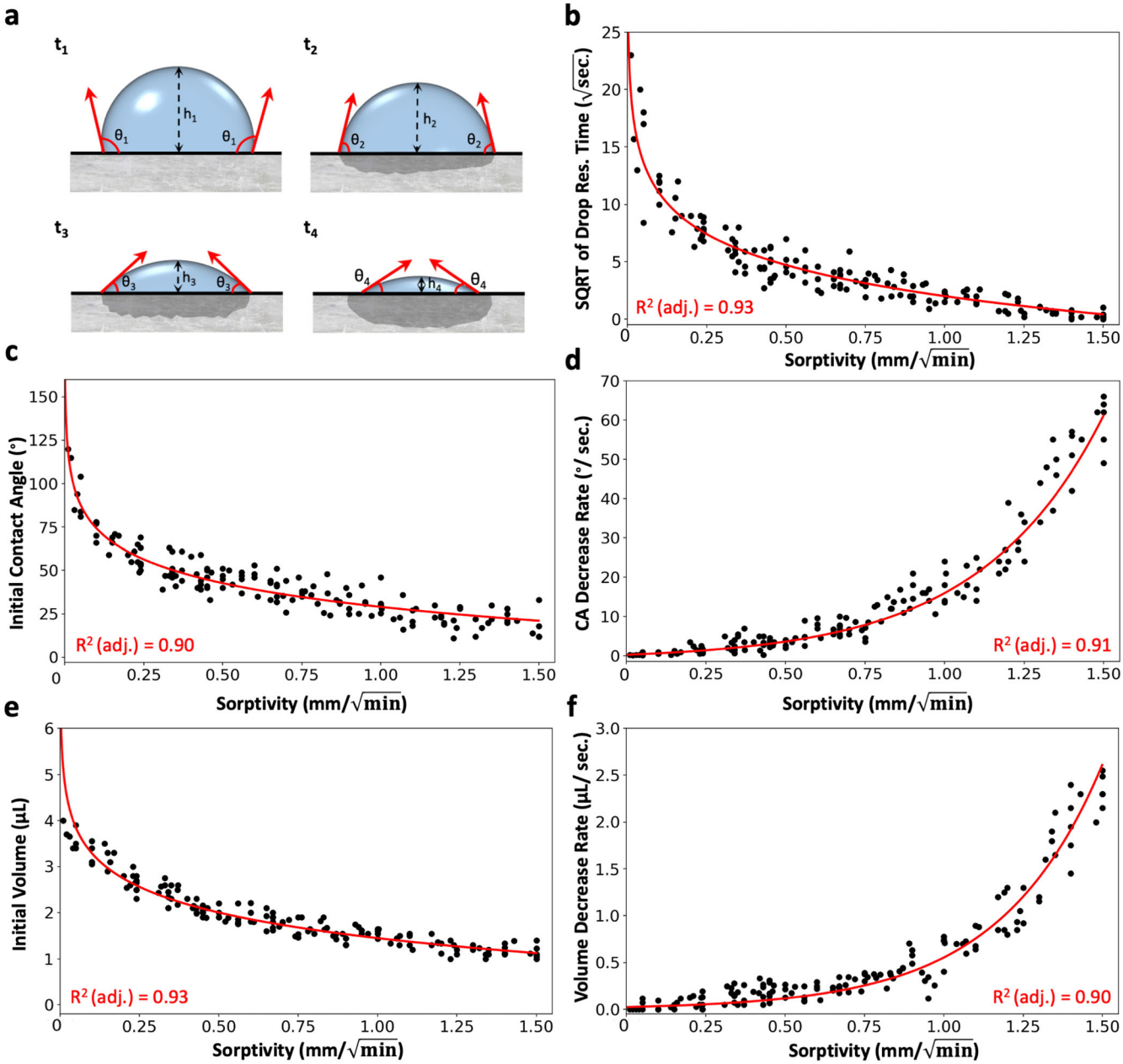

Fig. 5 Establishing the correlation between surface sorptivity and surface wettability. a A 2D schematic of drop spreading on a porous substrate at t_1 (0.5 s) to t_4 (i.e., arbitrary time), note that due to spherical cap estimations, the left and right CAs are assumed to be approximately similar, **b** establishing a strong logarithmic correlation between the square root of drop residence time and initial sorptivity, **c** a strong logarithmic correlation between initial CA (at 0.5 s) and initial sorptivity, **d** a strong exponential correlation between CA decrease rate and initial sorptivity, **e** a strong logarithmic correlation between initial volume and initial sorptivity, and (**f**) a strong exponential correlation between drop volume decrease rate and initial sorptivity. In summary, this figure shows that analyzing the dynamics of drop spreading is sufficiently accurate to estimate the sorptivity of cement pastes.

saturated limewater), the S_a, i.e., average roughness, and S_q, i.e., root mean square roughness, values remain unchanged for all specimens regardless of their curing periods. To justify this phenomenon, it can be argued that two surfaces can have similar average roughness (S_a) and root mean square roughness (S_q) values due to similar finishing techniques but differ in other roughness parameters such as valley depth, peak curvature, interfacial area ratio, valley void volume, and peak density. This is because surface roughness is a multi-dimensional property and additional parameters are needed to provide insight into specific aspects of texture and profile. Thus, despite similarities in overall roughness and height variations, these aspects can vary between surfaces. Hence, a complete evaluation of surface roughness parameters is necessary to fully understand the surface properties of cementitious materials, as S_a and S_q values alone are not sufficient. For this purpose, all 24 roughness parameters measured by the laser profilometer were analyzed, and correlations (R^2) were established between sorptivity and roughness parameters (see Supplementary Fig. 15). In addition, for similar indices, the correlations between the 24 roughness parameters and CA of cement pastes were determined and shown in Supplementary Fig. 16. Comparisons of Supplementary Figs. 15 and 16 reveal that two roughness indices can 'primarily' impact the CA values (Fig. 4). Essentially, Fig. 4 shows that an increase in the S_{vk}, i.e., average

mean of valley depth, or S_{dr}, i.e., developed interfacial area ratio, results in an improvement in the surface lubricating properties. A lower CA can lead to better wetting and the formation of a continuous lubricating film on the surface, which can help reduce friction and improve the surface's lubricating properties. For example, reducing the w/c ratio of cement paste reduces pore or void formation, leading to a smoother surface by promoting denser and more uniform particle packing. As a result, samples with lower w/c ratios (lower sorptivity) have smaller S_{vk}, and S_{dr} values but higher CAs (Fig. 4). The surface roughness of cement can also change with the curing period as the microstructure develops. Longer curing periods can result in smoother surfaces due to denser, homogeneous microstructures, while shorter periods can cause rougher surfaces from microcracks and pores. This means that samples exposed to shorter curing periods (higher sorptivity) have higher S_{vk} and S_{dr} values but smaller CAs (Fig. 4). It should be noted that apart from the 'primary' roughness parameters (shown in Fig. 4, with $R^2 > 0.95$), there are other parameters (correlated with primary indices, with smaller R^2 values) that also correlate with surface wettability properties. We define them as 'secondary' roughness indices (with $R^2 > 0.85$), summarized in Supplementary Fig. 17, which can also impact the surface wettability of pastes with different sorptivity values. Finally, the 24 roughness parameters introduced in Supplementary Figs. 15 and 16 were grouped according to their shared properties in Supplementary Table 1 explaining why the primary and secondary roughness parameters (introduced in Supplementary Fig. 17) are related.

It is further determined whether surface wettability measurements can reliably reflect the tendency of cementitious materials to absorb and transmit liquid via capillarity. For this reason, Supplementary Fig. 11b–f show the changes in the geometry of absorbing drops as a function of w/c ratios and moist curing periods. In particular, Supplementary Fig. 11b confirms that the square root of drop residence time, i.e., the time required for the drop to be fully absorbed on porous substrates ($h_i \rightarrow 0$ in Fig. 5a), amplifies for denser microstructures as they lack sufficient space to rapidly accommodate liquid bulk ingress. As a case in point, Supplementary Fig. 11b shows that the drop residence time varies from 250–400 s (square root of residence time = 15–20) if placed on a relatively dense substrate (e.g., w/c = 0.4, curing period = 7 days), but when placed on porous substrates (e.g., w/c = 0.8, curing period = 1 day) dramatically decreases to 0.5–2 s (square root of residence time = 0.7–1.4). The initial CA (i.e., measured at 0.5 s, θ_1 in Fig. 5a) is significantly larger on denser substrates for all specimens (Cem. A to C), see Supplementary Fig. 11c. To justify this phenomenon, it can be argued that apart from the surface tension of liquid drops (which is similar for all specimens), the capillary forces of substrates can significantly impact the geometry of drops, which is mainly controlled by the size and connectivity of the pore network[23].

As a result, when the substrate is denser, it has a lower surface energy and can provide stronger adhesive forces, leading to a larger CA. Supplementary Fig. 18 (calculated based on the OWRK model introduced in the methods section and Supplementary Appendix 2) confirms that decreased CA is associated with increased liquid wetting capability on the solid surface, implying elevated surface-free energy of the cement paste surfaces. However, it should be noted that indirect determination of surface free energy using CA measurements has potential problems. These include the selection of a theoretical model, the assumption of surface homogeneity, the impact of surface roughness, and the hysteresis effect that leads to inconsistent results and biased determinations of surface free energy. Moreover, as previously shown in Fig. 4, denser matrices, i.e., with lower w/c ratios and higher curing periods, have more homogeneous surfaces, resulting in less surface heterogeneity, i.e., smaller S_{vk}, and S_{dr} values. Put more simply, a decrease in these surface roughness parameters results in a smoother, more uniform surface with reduced irregularities and pockets for liquid adhesion, leading to increased CA due to decreased liquid spreading. Further, a reduction in these parameters results in fewer interaction sites for liquid molecules which leads to less wetting and a higher CA, i.e., liquid molecules have a greater tendency to remain cohesive and form droplets. Therefore, a decrease in S_{vk} and S_{dr} values causes the liquid to bead up which can likely increase the initial CA values. This explains why on dense (e.g., w/c = 0.4, curing period = 7 days) or porous (e.g., w/c = 0.8, curing period = 1 day) substrates, hydrophobicity or hydrophilicity patterns are observed, respectively.

When looking at Supplementary Fig. 11d, the average CA decrease rate ($[\theta_1 - \theta_4]/[t_4 - t_1]$ in Fig. 5a) is shown to amplify with an increase in the paste porosity, which could be attributed to surface roughness spreading and/or bulk penetration of liquid drops. However, the *smooth* samples have approximately similar root square roughness (Sq of 6–7.5 µm in Supplementary Figs. 12–S14), denoting that liquid bulk penetration plays a central role in controlling the average CA decrease rate. In fact, increased interactions and capillary forces on porous substrates cause the liquid to spread faster into the pores, which amplifies the CA decrease rate. Furthermore, Supplementary Fig. 11e, f shows that the initial drop volume (i.e., measured at 0.5 s based on Eq. 3) and average volume decrease rate ($[Vol_1 - Vol_4]/[t_4 - t_1]$ in Fig. 5a) are both a function of liquid bulk penetration, which is mainly influenced by paste porosity. This suggests that initial sorptivity can be potentially estimated by measuring the relative ease with which the drop can be absorbed by the cementitious matrix.

Subsequently, Fig. 5 establishes the correlations between initial sorptivity, and wettability parameters of pastes made with different cements (Cem. A to C, or Cem. A partially replaced with 5 wt. % silica fume), w/c ratios (0.4, 0.5, 0.6, 0.7, and 0.8), moist curing periods (1, 3, and 7 days), and surface roughness (rough or smooth). The schematic shown in Fig. 5a is a drop spreading time-lapse on a porous substrate, which is used to better describe many parameters including the changes in drop residence time (h_i), initial contact angle (θ_1), volume decrease rate ($[Vol_1 - Vol_4]/[t_4 - t_1]$), and CA decrease rate ($[\theta_1 - \theta_4]/[t_4 - t_1]$). Moreover, Fig. 5b establishes a strong logarithmic correlation between the initial sorptivity (mm/√min) and the square root of drop residence time (√sec), implying that the drops tend to stay longer on denser matrices. This phenomenon can be explained by the fact that the higher surface energy of denser matrices leads to stronger adhesive forces, which makes it harder for drops to detach and prolongs their lifetime/ residence time. Figure 5b also proves that regardless of surface roughness, all points would lie on the fitted line. Basically, although rougher (sandblasted) specimens have higher sorptivity values (marked by ASTM C1585 measurements, Fig. 3b) they absorb liquid faster compared to smoother surfaces (marked by wettability measurements, Fig. 3d), hence they would also remain on the fitted logarithmic line. It is worth noting that since the fitted *logarithmic* equation is nonlinear, estimating the R^2 value is not valid[52]. Therefore, an adjusted R^2 parameter is estimated by leveraging a method expressed in the literature for exponential (inverse of logarithmic) datasets[53].

Figure 5c fits a strong *logarithmic* correlation (adjusted $R^2 \geq 0.9$) between initial water repellence and initial sorptivity of cement pastes, proving that the initial CAs are in general larger on substrates of smaller porosity. Again, based on Fig. 3c, rougher surfaces have smaller CAs; however, since they have higher initial sorptivity than smoother substrates, their data points would also remain on the fitted logarithmic curve. As previously discussed, the initial CA of liquid drops is larger on denser (low sorptivity) substrates due to their lower surface energy and stronger adhesive forces. In addition, denser matrices have less surface heterogeneity (i.e., smaller S_{vk} and S_{dr} values) and fewer interaction sites for liquid molecules, resulting in increased CA

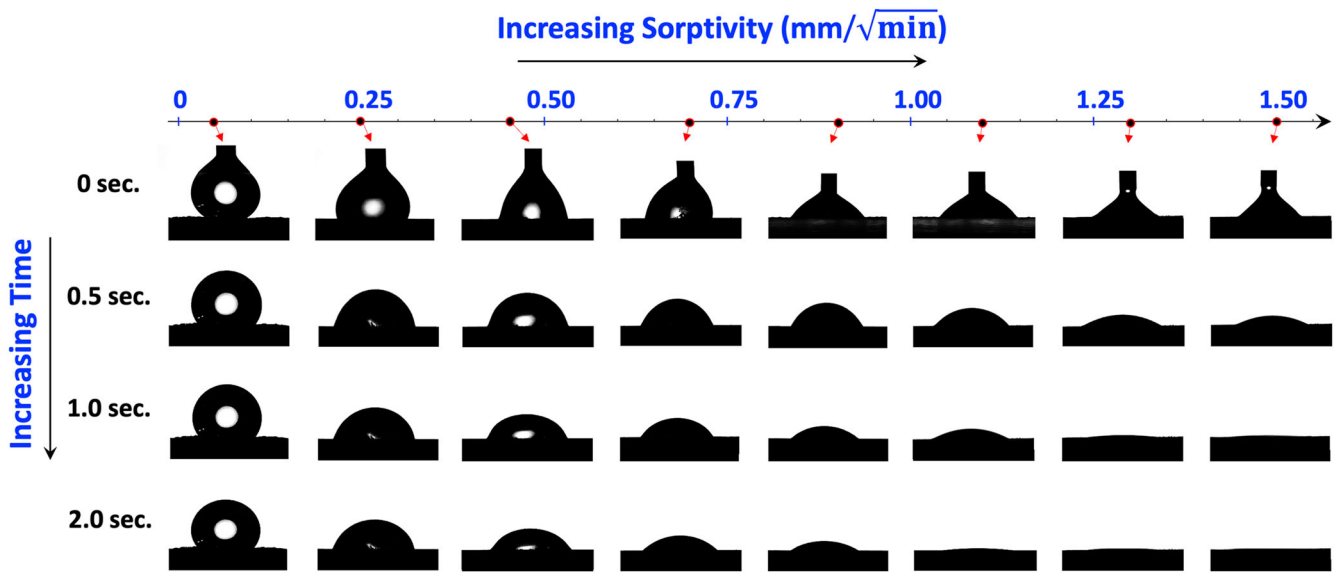

Fig. 6 Dynamics of drop spreading on surfaces of varying sorptivity. Time-lapse of drops on different absorbing surfaces as a function of time (0–2 s) and sorptivity (0–1.5 mm/√min). This figure confirms that for surfaces of lower sorptivity, the initial CAs, initial volumes, and residence times are larger, while the absorption, CA decrease rate, and volume decrease rates are smaller.

due to reduced liquid spreading and increased droplet formation. Figure 5d shows that regardless of cement type, curing regime, w/c ratio, or surface roughness, the CA decrease rate amplifies exponentially (adjusted $R^2 \geq 0.9$) with an increase in initial sorptivity due to the higher rate of liquid infiltration in more porous substrates. In fact, this increased infiltration rate leads to a larger CA decrease rate as more surface sites become available for wetting.

Apart from estimating the CA values, Fig. 5e relates the initial volume of drops (measured at 0.5 s) with the initial sorptivity using a logarithmic function, proving that the volume of *as-placed* drops remains unchanged (~4 μL) on denser matrices (e.g., w/c = 0.4, curing period = 7 days), while rapidly decreasing to ~1 μL on porous microstructures (e.g., w/c = 0.8, curing period = 1 day). Basically, the lower surface porosity of denser substrates reduces the number of sites for drop penetration, which maintains the drop's initial volume. Interestingly, the initial CA (Fig. 5c) and initial drop volume (Fig. 5e) are proportional for different sorptivity values denoting that the liquid bulk ingress into the cementitious matrix can largely control the overall sorptivity of drops.

To further illuminate the correlation between initial water repellence and initial drop volume, Video 2 shows how the initial CAs decrease with an increase in sorptivity, due to surface capillary forces. In addition, Video 2 shows how an ellipsoidal wetted region is extended during the accommodation of liquid ingress and associates lower initial drop volume with increased sorptivity. The rate of water absorption decreases with time for a dense matrix as the wetting front encounters the increasingly saturated zone. As shown in Fig. 5f, the average volume decrease rate amplifies exponentially with an increase in the initial sorptivity of substrates. In other words, the relative amount of absorbed drop volume can fully capture the absorption rate of different cementitious substrates. Comparisons of Fig. 5d, f verify that the ratio of the CA decrease rate ($\Delta CA = [\theta_1 - \theta_4]/[t_4 - t_1]$ in Fig. 5a) to the volume decrease rate ($\Delta V = [Vol_1 - Vol_4]/[t_4 - t_1]$ in Fig. 5a) revolves around a constant range of $K = \Delta CA/\ \Delta V = 0.75\ -1.25°$ (see Supplementary Fig. 19). This proves that regardless of surface sorptivity, the CA constantly decreases for each percentage of drop volume absorbed into the paste microstructure.

Finally, Fig. 6 provides a time-lapse of absorbing drops on cementitious surfaces of varying porosity/sorptivity, which systematically summarizes the findings of Fig. 5. Similarly, Video 3 shows the spreading of back-lit illuminated drops on surfaces with different rates of absorption. Both Fig. 6 and Video 3 suggest that for a denser matrix (where Sorptivity, $S \leq 0.05$ mm/√min), the initial CA, initial volume, and residence time are relatively high; subsequently, the rate of liquid absorption, volume decrease rate, and CA decrease rate would be low. On the other hand, for a more porous matrix (e.g., $S \geq 1.0$ mm/√min), the initial CA, initial volume, and residence time are relatively low; hence, the rate of absorption, volume decrease rate, and CA decrease rate would be high. Finally, selected surface roughness parameters obtained from a laser profilometer (see Fig. 4 and Supplementary Fig. 17) are found to be strongly correlated to CA measurements as well as sorptivity values—which are linked to other durability indices of cement-based systems (see Supplementary Table 2). In summary, surface wettability measurements can be efficiently leveraged to rapidly, reliably, and economically estimate the penetration tendency of liquids into cementitious systems of varying compositions and porosities.

Limitations

As shown in this study, accurate and rapid estimation of initial sorptivity is possible using surface wettability measurements. However, there are a few technical limitations of the proposed methodology which can be subject to future improvements. Firstly, the CA measurements proposed here (which take a few minutes to accomplish) are found to be correlated only with the initial sorptivity values and not the secondary sorptivity values of the system. This observation is likely because this rapid test is based on capillary absorption, and thus cannot be used to estimate the secondary sorptivity (moisture diffusion through gel pores) of cementitious materials. Secondly, we primarily focused on cementitious pastes for this initial exploration; hence, our findings are limited to binders and paste systems. Whether such experiments can be extended to concrete samples or not remains to be seen. Thirdly, our study focused on investigating the influence of surface roughness and capillary forces of substrates on CA measurements. However, it is crucial to note that surface energy is determined by a combination of capillary forces, surface roughness, and chemical components such as ions (e.g., Ca^{2+}) or polar groups (e.g., OH^-). Although we did not measure the role of

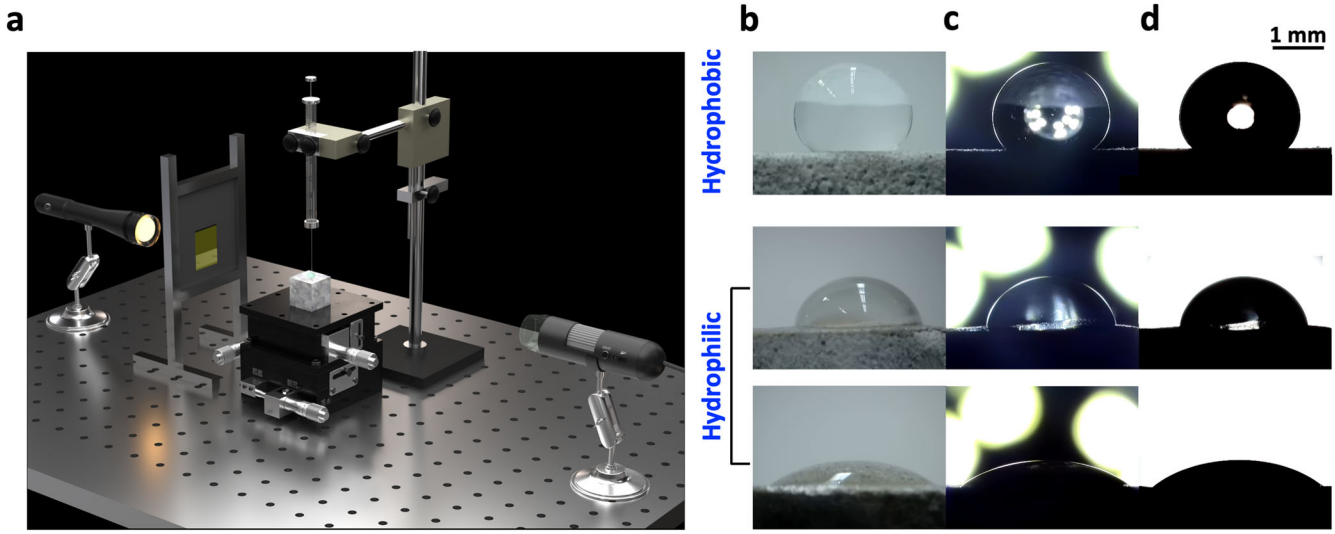

Fig. 7 Measuring drop geometry on cementitious substrates. a A 3D schematic of the sessile drop goniometry. Hydrophilicity and hydrophobicity surface patterns illuminated by (**b**) normal room lighting condition, (**c**) back-lit setup where the diffuser filter is absent, and (**d**) back-lit setup where the diffuser filter is present, and bi-tonal images have resulted.

chemical parameters in our study, we acknowledge their potential influence. In spite of these three limitations, we believe that wettability measurements can pave the path for rapid estimation and prediction of cementitious sorptivity, and consequently provide an ultra-fast indication of cementitious durability. Moreover, Fig. 4 confirms the existence of a strong linear correlation between roughness parameters S_{vk} (or S_{dr}) and sorptivity values. This raises the interesting aspect of whether surface roughness characterization alone would suffice for predicting sorptivity—an issue that should be further explored in future studies. However, the laser profilometer (used for measuring all roughness indices) comes with a considerably high capital cost, which limits its widespread adoption. Consequently, we determined that CA measurements (that exhibit nonlinear correlations with sorptivity values) can provide a faster and more inexpensive way of assessing the absorption rate of cementitious systems. In line with this aspect, we have recently proposed a CA goniometer developed in our lab which cost less than $200[54].

METHODS

Test specimens

Paste cubes, 10 × 10 × 10 mm, were cast in silicone molds by mixing materials at water-to-cement (w/c) ratios of 0.4, 0.5, 0.6, 0.7, and 0.8 in 50 mL polypropylene centrifuge tubes in a vortex mixer running continuously at 3000 rpm for 2 min. The samples were hardened and demolded after 24 h of moist curing inside a sealed container over water (23 °C and 95% RH). In selected mixes (cement type = A, w/c = 0.8) the cement was partially replaced with silica fume (by 5 wt.%) to further generalize the findings of this study. Followed by 24 h of curing, part of the paste specimens was immediately stopped from hydrating, while the rest were kept in saturated lime water (1.5 g of $Ca(OH)_2$ dissolved in a liter of deionized water at 23 °C) for 3 and 7 days. To cease cement hydration at desired ages, samples were immersed in isopropyl alcohol for 48 h and the solution was replaced every 12 h. In the next step, the samples were removed from alcohol and stored in a 23 °C vacuum chamber over silica gel (to absorb moisture) and soda-lime pellets (to absorb CO_2) for 14 days until a constant mass was achieved[55]. To perform the water absorption test, the paste cubes were sealed on five sides, and the sixth (unsealed) face was exposed to water. For surface wettability measurements, the surfaces were not sealed with epoxy, and the four faces of the cubic specimens that were touching the walls of the silicone molds (with no additional surface preparations and approximately similar global roughness properties) were subjected to surface wettability measurements. Supplementary Table 3 summarizes the chemical compositions and physical properties of three ASTM type 1 ordinary Portland cements and silica fume for casting and molding paste cubes.

Measuring rate of absorption

The absorption of paste samples was measured in accordance with ASTM C1585[14], i.e., the incremental mass change of specimens through unsaturated flow was recorded at higher frequencies during the first 6 h (i.e., time points of 2, 5, 10, 15, 20, 30, 45, 60, 75, 90, 120, 180, 240, and 360 min) of solid-liquid interaction, see Supplementary Fig. 9 in the Supporting Information. The amount of absorbed water is normalized as follows:

$$i = \frac{m}{a\rho} \tag{4}$$

where m is the mass change with time, a is the exposed area (i.e., unsealed face) of the specimen that touches water, ρ is the water density (~1000 kg.m^{-3} at 23 °C), and i is the normalized cumulative fluid volume that has been unidirectionally absorbed by the specimen, i.e., called *penetration*. Next, by plotting the penetration versus the square root of time (Supplementary Fig. 10), the initial sorptivity is estimated by calculating the slope of the first fitted linear line using the least square method, and its linearity is justified by the diffusion equation through Boltzmann's Transformation, shown by the following linear differential equation[16,56,57]:

$$\frac{\partial \varphi(r,t)}{\partial t} = D\nabla^2\varphi(r,t) \tag{5}$$

where ∇^2 is the Laplace operator, $\varphi(r, t)$ is the density of the diffusing cementitious material at time t and location r, and D is a constant diffusion coefficient. Also, the fitted line can have a small positive intercept that corresponds to the filling of the open porosity when the unsealed face of the sample comes in contact with water. Considering the papers referenced in Supplementary Table 4, sorptivity may only pertain to initial sorptivity and the time interval used to fit a regression line for estimating the initial sorptivity values can vary (from 16 to 400 min) depending on the linearity of the dataset. Also, the sorptivity values largely depend

on the initial water content of the specimens, which is controlled by the conditioning method or the drying procedure/temperature[58]. Interestingly, due to the relatively small dimension of the tested paste cubes (<10 mm), changing the drying temperature from 23 °C to 50 °C would not impact the sorptivity values; nonetheless, a further increase in the temperature (i.e., to 105 °C) was avoided as it changes the pore microstructure (i.e., induces microcracking) and negatively impacts the results, see Supplementary Fig. 20.

Measuring the level of background noise

To determine whether the back-lit illuminated drops are focused, the ratio of the desired signal (liquid phase) to the level of background noise (gas phase) was measured based on the first derivative of pixels grayscale values along a single line that passes through the drop. This measurement is denoted here as signal-to-noise ratio (SNR) and is expressed in decibels (dB) as follows[59]:

$$\mathrm{SNR(dB)} = 20\log_{10}\left(\frac{A_{signal}}{A_{noise}}\right) \tag{6}$$

where A is the root mean square (RMS) amplitude of the signal. It should be noted that an absolute SNR of at least 20 dB corresponds to a focused image denoting that the background noise is at a local minimum and the signal is clearly readable, see Video 1. In particular, this video shows that as the camera lens was gently moved away from the drop, the corresponding SNR was measured for each video frame to accurately determine the camera position that yields focused images.

Goniometer setup

CA measurements were done by a sessile drop goniometry[60], which comprises a USB microscopy camera (10 µm spatial resolution and frame rate of 20 fps), adjustable and leveled XYZ–mechanical stage, external light source, diffuse filter, and liquid dispenser, i.e., pipette or syringe, see Fig. 7a. In normal room lighting condition (Fig. 7b), the light transition between the drop and its background is not sharp enough to accurately delineate the region of interest (ROI). Therefore, the drop was located between the light source and the camera lens for a higher contrast back-lit illumination. In addition, a diffuser filter was placed in front of a specular light source to remove bright spots (Fig. 7c) from the imagery data and to create bi-tonal (black and white) images (Fig. 7d). The focused drop images were then analyzed by fitting a tangent line to the drop boundary at the ternary phase contact point. The goniometer was located in an area that has no organic vapors, dust, or vigorous air movement, and was exposed to a constant relative humidity (50 ± 5%) and temperature (23 ± 1 °C). In fact, as long as the ambient temperature remains within 20–40 °C, the surface tension of water would not change[61]. Finally, the sturdy and vibration-free mechanical stage, which faces the camera, was manually leveled as a small (out-of-plane) tilting angle of <4.5° in the camera view could dramatically reduce the SNR at the solid-liquid interface and impose systematic error, see Supplementary Fig. 21. As shown in Supplementary Table 5, the user has to do a one-time calibration on the goniometer, which normally takes 8–11 min, then the measurements can be done in 7–18 min for each specimen.

Drop placement on solid surfaces

To limit drop distortion, the syringe needle and pipette tip were placed in close proximity to the sample i.e., <2.5 mm from the surface, such that the tip of the liquid dispenser was embedded in the liquid. As Video 4 suggests, a further increase in the distance of the dispenser from the solid surface (i.e., distance >2.5 mm) would suspend the drop, leading to a non-trivial change in the drop geometry, especially for a hydrophilic surface. Hence, for all experiments, we chose a distance of less than 2.5 mm between the tip of the dispenser and the solid surface. In the next step, 4 ± 0.2 µL or 10 ± 0.2 µL of deionized water, i.e., with a calculated viscosity of 1.004 (mPa s) and calculated surface tension of 71.99 mN·m^{-1} was gently placed on the surface of paste specimens for CA measurements. The dynamic viscosity (µ) of deionized water changes with temperature, which is estimated using the equation below[62,63]:

$$\mu(^{\circ}K, mPa.s) = A(mPa.s) \times 10^{\left(\frac{B(^{\circ}K)}{T(^{\circ}K)-C(^{\circ}K)}\right)} \tag{7}$$

where, $A = 2.414 \times 10^{-3}$, $B = 247.8$, $C = 140$, and T is the ambient temperature. Similarly, the surface tension (σ) of deionized water is estimated as follows[64]:

$$\sigma\left(\frac{N}{m}\right) = B\left(10^{-3}\frac{N}{m}\right) \cdot \left[\frac{T_c(^{\circ}K) - T(^{\circ}K)}{T_c(^{\circ}K)}\right]^{\mu} \cdot \left(1 + b \cdot \left[\frac{T_c(^{\circ}K) - T(^{\circ}K)}{T_c(^{\circ}K)}\right]\right) \tag{8}$$

where, $B = 235.8$, $b = -0.625$, $T_c = 647.15$, and $\mu = 1.256$. Supplementary Fig. 22a shows the laboratory temperature ranging from ~22 to 24 °C, and based on Eqs. 7 and 8, the fluctuations in water's viscosity and surface tension are limited to approximately 3%, having a negligible impact on wettability measurements. However, relative humidity can have more impact on the CA values when compared to temperature. Supplementary Fig. 22b confirms that airflow can potentially decrease local relative humidity from 52% to 21%, resulting in rapid drop evaporation that can reduce the CA values from 128° to 97°. It should be noted that drops dispensed on non-absorbing, hydrophobic, and isotropic surfaces show higher evaporation under RH < 50% while limiting the RH value to 60% can also reduce the possibility of the condensation phenomenon[65,66].

After 10 wettability measurements, the pipette tip or syringe needle was cleaned or replaced as the impurities in the liquid can significantly impact the reproducibility of results and impose random error[67]. It is worth noting that the initial or as-placed CA measurements were started at 0.5 s from the onset of solid-liquid interaction to avoid misinterpretation of oscillating hydrophobic or hydrophilic drop boundaries (i.e., |SNR|>20 dB at the liquid-solid interface), shown in Video 5. Considering this video, the back-light image of drops stabilizes in less than 0.1 s on hydrophilic surfaces. In contrast, on hydrophobic surfaces, it can take 5x longer, i.e., ~0.5 s, to reach equilibrium. Hence, all measurements in our study were initiated at 0.5 s after the solid-liquid interaction onset. In addition, due to surface heterogeneities and inhomogeneities[68], at least 6 measurements were recorded from each specimen to get a range of metastable CAs on nonideal cementitious substrates[69]. It is worth noting that measuring equilibrium or receding CA on porous surfaces is not possible[70], hence the dynamic CA analysis was leveraged to continuously study the changes in the geometry (i.e., height, and radius), volume, and CA of moving drops[71]. Furthermore, surface wettability assessments were done over virgin and vacuum-dried specimens, and the duration of each experiment was limited (<10 min) to eliminate liquid evaporation and to generate meaningful/reproducible CA data.

Fitting algorithm for boundary detection and tangent line estimations

The cubic spline fitting algorithm was leveraged to specify the drop profile through the sharp contrast gradient between the liquid and its background, i.e., the gas phase. In this method, there is no assumption about the drop shape, and a cubic polynomial line is locally fitted between two neighboring points, i.e., $(x_i, f(x_i))$ and $(x_{i-1}, f(x_{i-1}))$, specified by the user. Then the cubic equation

on each interval is derived and expressed as follows[72]:

$$f_i(x) = \frac{f_i''(x_{i-1})}{6(x_{i-1}-x_i)}(x_i - x)^3 + \frac{f_i''(x_i)}{6(x_i - x_{i-1})}(x - x_{i-1})^3 + \left[\frac{f(x_{i-1})}{x_i - x_{i-1}} - \frac{f_i''(x_{i-1})(x_i - x_{i-1})}{6}\right](x_i - x) + \left[\frac{f(x_i)}{x_i - x_{i-1}} - \frac{f_i''(x_i)(x_i - x_{i-1})}{6}\right](x - x_{i-1}) \quad (9)$$

where, $f_i''(x_{i-1})$ and $f_i''(x_i)$ are the 2nd derivatives of the cubic function at the end of each interval. For selected points, the function values, and their 1st and 2nd derivatives are equal at the interior points. The first and last functions should pass through the global endpoints with zero 2nd derivative. Moreover, the user can sufficiently improve the accuracy of results by increasing the number of points (N) and decreasing the numerical step size ($\Delta h = x_i - x_{i-1}$). It is worth noting that the baseline (the contact line between the gas, liquid, and solid phases of a 2D image) has to be manually specified and coupled with the fitted cubic spline polynomial to measure the tangent line at the ternary phase contact points. In addition, Supplementary Appendix 3 contains the Python code employed that leverages the cubic spline fitting algorithm for quantifying the CA of hydrophilic drop images.

Surface roughness analysis

A Keyence VK-X1000 profilometer, with a 405 nm laser, 20 nm vertical resolution, and 120 nm lateral resolution analyzing 2100 µm by 2500 µm rectangular areas, was used to provide the contour height map of the ROI and subsequently measure surface roughness through confocal scanning. In addition, the tilting angle of the profile graph was manually corrected to display a leveled height map. To better characterize the surface roughness of different paste specimens, average height, average roughness (S_a), root mean square roughness (S_q), average valley depth (S_{vk}), and interfacial area ratio (S_{dr}) dispersion parameters (as well as other roughness indices) were estimated using the measured contour height map $h_{(x,\ y)}$ of a rectangular area (ROI) that has a length of L and width of W[73–75]:

$$\text{Average Height} = \frac{1}{LW}\int_0^W\int_0^L h_{(x,y)}\,dx\,dy \quad (10)$$

$$\text{Average Roughness } (S_a) = \frac{1}{LW}\int_0^W\int_0^L \left|h_{(x,y)}\right|dx\,dy \quad (11)$$

$$\text{Root Mean Square Roughness } (S_q) = \left[\frac{1}{LW}\int_0^W\int_0^L {h_{(x,y)}}^2\,dx\,dy\right]^{\frac{1}{2}} \quad (12)$$

$$\text{Interfacial Area Ratio } (S_{dr}) = \frac{1}{LW}\left(\int_0^W\int_0^L\left[1 + \left(\frac{\partial h_{(x,y)}}{\partial x}\right)^2 + \left(\frac{\partial h_{(x,y)}}{\partial y}\right)^2\right]^{\frac{1}{2}} - 1\right)dx\,dy \quad (13)$$

Surface free energy measurements

To calculate the surface free energy of cement pastes of varying compositions and curing histories, the OWRK model (with dispersive 'D' and polar 'P' components) was implemented[76]. The OWRK model equations typically involve a set of linear equations that relate the surface free energy components to the CAs. The equations incorporate parameters specific to two polar liquids (e.g., water and glycerol) to calculate the polar and dispersive components of the solid as follows:

$$\frac{\gamma_L(1+\cos\Theta)}{2} = \left(\gamma_L^D \cdot \gamma_S^D\right)^{0.5} + \left(\gamma_L^P \cdot \gamma_S^P\right)^{0.5} \quad (14)$$

$$\gamma_L = \gamma_L^D + \gamma_L^P \quad (15)$$

$$\gamma_S = \gamma_S^D + \gamma_S^P \quad (16)$$

where γ_L represents the overall surface tension of the liquid, γ_L^D represents the dispersive component of the liquid's surface tension, γ_L^P represents the polar component of the liquid's surface tension, γ_S represents the overall surface energy of the solid, γ_S^D represents the dispersive component of the solid's surface energy, γ_S^P represents the polar component of the solid's surface energy, and Θ represents the CA that the liquid makes on the solid surface. The dispersive and polar components of water's surface tension are 26.4 and 46.4 mN.m^{-1} respectively, and corresponding values for glycerol are 37 and 26.4 mN.m^{-1} respectively (values taken from Rulison's paper)[77]. Following, these equations (i.e., Eqs. 14–16) are solved to estimate the surface free energy values based on the CAs. Our Supplementary Appendix 2 provides a detailed demonstration of how the OWRK method can be implemented to estimate the surface-free energy of cement pastes.

Raman imaging

The Raman spectra were acquired using the WITec Alpha 300 series SNOM confocal microscope. With this device, we captured a 1 mm × 1 mm area using a 523 nm laser, with a resolution of 10 µm.pixel^{-1}, a 20X objective lens, 10 mW excitation power, and a 600 gr.mm^{-1} grating, covering a wavenumber range of 200–4000 cm^{-1}. We selected the 3620 cm^{-1} wavenumber to observe the OH^- stretching vibration. The integration time was set to 0.5 s, resulting in a total scanning time of 1.5 h. By stitching together 16 subplots, we generated a $Ca(OH)_2$ phase map. The raw data underwent preprocessing steps, including cosmic ray removal (filter size of 2, dynamic factor of 8), baseline correction, normalization of the maximum intensity peak to 1, and true component analysis with external reference spectra on WITec's Project FIVE software. For thresholding the phase map, we utilized the IsoData algorithm available in ImageJ. Our group's recent publications detail the comprehensive procedure we employ for stitching and analyzing large-area Raman images which are representative of a variety of cementitious systems[78,79].

DATA AVAILABILITY

All data supporting the findings of the present study are available within the article and the Supplementary Information (SI). Additional data is available upon request from the corresponding author.

CODE AVAILABILITY

The Python codes can be accessed in the Supplementary Appendix 1-3 of the manuscript. Additional codes are available upon request from the corresponding author.

Received: 24 February 2023; Accepted: 9 June 2023;
Published online: 05 July 2023

REFERENCES

1. Habert, G. et al. Environmental impacts and decarbonization strategies in the cement and concrete industries. *Nat. Rev. Earth Environ.* **1**, 559–573 (2020).
2. Angst, U. M. & Elsener, B. The size effect in corrosion greatly influences the predicted life span of concrete infrastructures. *Sci. Adv.* **3**, e1700751 (2017).

3. Maltais, Y., Samson, E. & Marchand, J. Predicting the durability of Portland cement systems in aggressive environments—Laboratory validation. *Cem. Concr. Res.* **34**, 1579–1589 (2004).
4. Krus, M., Hansen, K. K. & Künzel, H. M. Porosity and liquid absorption of cement paste. *Mater. Struct.* **30**, 394–398 (1997).
5. Buenfeld, N. R. & Newman, J. B. Examination of three methods for studying ion diffusion in cement pastes, mortars and concrete. *Mater. Struct.* **20**, 3–10 (1987).
6. Banthia, N. & Mindess, S. Water permeability of cement paste. *Cem. Concr. Res.* **19**, 727–736 (1989).
7. Hall, C., & Hoff, W. D. *Water tRansport in Brick, Stone and Concrete* (CRC Press, 2021).
8. ASTM C1202 – 22. American Society for Testing and Materials, Standard Test Method for Electrical Indication of Concrete's Ability to Resist Chloride Ion Penetration. *Annual Book of ASTM Standards, V.04.01* (ASTM International, Pennsylvania, 2022).
9. AASHTO, T 358 – 21, *Standard Method of Test for Surface Resistivity Indication of Concrete's Ability to Resist Chloride Ion Penetration (*American Association of State Highway and Transportation Officials, Washington, D.C., US, 2021).
10. AASHTO, T 259 – 21, *Standard Method of Test for Resistance of Concrete to Chloride Ion Penetration* (American Association of State Highway and Transportation Officials, Washington, D.C., US, 2021).
11. ASTM C1556 – 11a. American Society for Testing and Materials, Standard Test Method for Determining the Apparent Chloride Diffusion Coefficient of Cementitious Mixtures by Bulk Diffusion. *Annual Book of ASTM Standards, V.04.01* (ASTM International, Pennsylvania, 2016).
12. NT BUILD 492, Concrete, mortar and cement-based repair materials: chloride migration coefficient from non-steady-state migration experiments. *Nordic Council of Ministers* **1**, 1–8 (1999).
13. EN 12390 – 8, B. S. Testing hardened concrete-Part 8: Depth of penetration of water under pressure (2019).
14. ASTM C1585 – 20. American Society for Testing and Materials, Standard Test Method for Measurement of Rate of Absorption of Water by Hydraulic-cement Concretes. *Annual Book of ASTM Standards, V.04.01* (ASTM International, Pennsylvania, 2020).
15. Henkensiefken, R., Castro, J., Bentz, D., Nantung, T. & Weiss, J. Water absorption in internally cured mortar made with water-filled lightweight aggregate. *Cem. Concr. Res.* **39**, 883–892 (2009).
16. Hall, C. Water sorptivity of mortars and concretes: a review. *Mag. Concr. Res.* **41**, 51–61 (1989).
17. Martys, N. S. & Ferraris, C. F. Capillary transport in mortars and concrete. *Cem. Concr. Res.* **27**, 747–760 (1997).
18. Lockington, D., Parlange, J. Y. & Dux, P. Sorptivity and the estimation of water penetration into unsaturated concrete. *Mater. Struct.* **32**, 342–347 (1999).
19. Liu, Z. et al. Experimental and simulation study of water absorption in unsaturated concrete. *J. Mater. Civ. Eng.* **33**, 04021332 (2021).
20. Zhutovsky, S. & Hooton, R. D. Role of sample conditioning in water absorption tests. *Constr. Build. Mater.* **215**, 918–924 (2019).
21. Sabir, B. B., Wild, S. & O'farrell, M. A water sorptivity test for mortar and concrete. *Mater. Struct.* **31**, 568–574 (1998).
22. Lafuma, A. & Quéré, D. Superhydrophobic states. *Nat. Mater.* **2**, 457–460 (2003).
23. Neogi, P. & Miller, C. A. Spreading kinetics of a drop on a rough solid surface. *Colloid Interface Sci.* **92**, 338–349 (1983).
24. Davis, S. H. & Hocking, L. M. Spreading and imbibition of viscous liquid on a porous base. *Phys. Fluids* **11**, 48–57 (1999).
25. Zheng, M. et al. Influence of porous high entropy alloy coating on wetting behavior and interfacial microstructure of al-si alloy on steel substrate. *J. Alloys Compd*. **912**, 165154 (2022).
26. Marmur, A., Della Volpe, C., Siboni, S., Amirfazli, A. & Drelich, J. W. Contact angles and wettability: towards common and accurate terminology. *Surf. Innov.* **5**, 3–8 (2017).
27. Law, K. Y. Definitions for hydrophilicity, hydrophobicity, and superhydrophobicity: getting the basics right. *J. Phys. Chem. Lett.* **5**, 686–688 (2014).
28. Isimjan, T. T., Wang, T. & Rohani, S. A novel method to prepare superhydrophobic, UV resistance and anti-corrosion steel surface. *J. Chem. Eng.* **210**, 182–187 (2012).
29. Sharma, R. & Garg, N. Superhydrophobic and self-cleaning aluminum via a rapid and controlled process. *ACS Appl. Energy Mater*. **1**, 417–427 (2022).
30. Sun, T., Feng, L., Gao, X. & Jiang, L. Bioinspired surfaces with special wettability. *Acc. Chem. Res.* **38**, 644–652 (2005).
31. Lee, J. B., Derome, D. & Carmeliet, J. Drop impact on natural porous stones. *J. Colloid Interface Sci.* **469**, 147–156 (2016).
32. Grüßer, M., Waugh, D. G., Lawrence, J., Langer, N. & Scholz, D. On the droplet size and application of wettability analysis for the development of ink and printing substrates. *Langmuir* **35**, 12356–12365 (2019).
33. Xu, Z. N. An algorithm for selecting the most accurate protocol for contact angle measurement by drop shape analysis. *Rev. Sci. Instrum.* **85**, 125107 (2014).
34. Semprebon, C. & Brinkmann, M. On the onset of motion of sliding drops. *Soft Matter* **10**, 3325–3334 (2014).
35. Stalder, A. F., Kulik, G., Sage, D., Barbieri, L. & Hoffmann, P. A snake-based approach to accurate determination of both contact points and contact angles. *Colloids Surf. A Physicochem. Eng. Asp.* **286**, 92–103 (2006).
36. Xu, Z. N. A noise-resistant ADSA-PH algorithm for superhydrophobic surface's static contact angle evaluation. *AIP Adv.* **7**, 035210 (2017).
37. García, G. B. et al. *Learning image processing with OpenCV*. (Packt Publishing, Birmingham, 2015).
38. Cassie, A. B. D. & Baxter, S. Wettability of porous surfaces. *J. Chem. Soc., Faraday Trans.* **40**, 546–551 (1944).
39. Kamusewitz, H., Possart, W. & Paul, D. The relation between Young's equilibrium contact angle and the hysteresis on rough paraffin wax surfaces. *Colloids Surf. A Physicochem. Eng. Asp.* **156**, 271–279 (1999).
40. Marmur, A. Solid-surface characterization by wetting. *Annu. Rev. Mater. Res.* **39**, 473–489 (2009).
41. Meiron, T. S., Marmur, A. & Saguy, I. S. Contact angle measurement on rough surfaces. *J. Colloid Interface Sci.* **274**, 637–644 (2004).
42. Holman, R. K., Cima, M. J., Uhland, S. A. & Sachs, E. Spreading and infiltration of inkjet-printed polymer solution droplets on a porous substrate. *J. Colloid Interface Sci.* **249**, 432–440 (2002).
43. Gu, H. et al. Investigation on contact angle measurement methods and wettability transition of porous surfaces. *Surf. Coat. Technol.,* **292**, 72–77 (2016).
44. Kumar, S. M. & Deshpande, A. P. Dynamics of drop spreading on fibrous porous media. *Colloids Surf. A Physicochem. Eng. Asp.* **277**, 157–163 (2006).
45. Harris, J. W. & Stöcker, H. Handbook of mathematics and computational science (Springer Science & Business Media, 1998).
46. Roberts, R., Senden, T. & Knackstedt, M. Spreading of aqueous liquids in unsized papers is by film flow. *J. Pulp Pap. Sci.* **29**, 123–131 (2003).
47. Miller, B. & Tyomkin, I. Liquid porosimetry: new methodology and applications. *J. Colloid Interface Sci.* **162**, 163–170 (1994).
48. Pasandideh-Fard, M., Qiao, Y. M., Chandra, S. & Mostaghimi, J. Capillary effects during droplet impact on a solid surface. *Phys. Fluids* **8**, 650–659 (1996).
49. Toivakka, M. Numerical investigation of droplet impact spreading in spray coating of paper. *Spring Adv. Coat. Fundam. Symp*. (2003).
50. DeSouza, S. J., Hooton, R. D. & Bickley, J. A. Evaluation of laboratory drying procedures relevant to field conditions for concrete sorptivity measurements. *Cem. Concr. Aggreg.* **19**, 59–63 (1997).
51. Parrott, L. J. Moisture conditioning and transport properties of concrete test specimens. *Mater. Struct.* **27**, 460–468 (1994).
52. Cameron, A. C. & Windmeijer, F. A. An R-squared measure of goodness of fit for some common nonlinear regression models. *J. Econom.* **77**, 329–342 (1997).
53. Ricci, L. Adjusted R-squared type measure for exponential dispersion models. *Stat. Probab. Lett.* **80**, 1365–1368 (2010).
54. Kabir, H. & Garg, N. Machine learning enabled orthogonal camera goniometry for accurate and robust contact angle measurements. *Sci. Rep.* **13**, 1497 (2023).
55. Zhang, J. & Scherer, G. W. Comparison of methods for arresting hydration of cement. *Cem. Concr. Res.* **41**, 1024–1036 (2011).
56. Khader, M. M. On the numerical solutions for the fractional diffusion equation. *Commun. Nonlinear Sci. Numer. Simul.* **16**, 2535–2542 (2011).
57. Pavlík, Z., Žumár, J., Pavlíková, M. & Černý, R. A Boltzmann transformation method for investigation of water vapor transport in building materials. *J. Build. Phys.* **35**, 213–223 (2012).
58. Castro, J., Bentz, D. & Weiss, J. Effect of sample conditioning on the water absorption of concrete. *Cem. Concr. Compos.* **33**, 805–813 (2011).
59. Kieser, R., Reynisson, P. & Mulligan, T. J. Definition of signal-to-noise ratio and its critical role in split-beam measurements. *ICES Mar. Sci.* **62**, 123–130 (2005).
60. Susana, L., Campaci, F. & Santomaso, A. C. Wettability of mineral and metallic powders: applicability and limitations of sessile drop method and Washburn's technique. *J. Powder Technol.* **226**, 68–77 (2012).
61. Zhao, Q., Liu, Y. & Abel, E. W. Effect of temperature on the surface free energy of amorphous carbon films. *J. Colloid Interface Sci.* **280**, 174–183 (2004).
62. Munson, B. R., Okiishi, T. H., Huebsch, W. W. & Rothmayer, A. P. *Fluid Mechanics* (pp. 271–274) (Wiley, Singapore, 2013).
63. Popiel, C. O. & Wojtkowiak, J. Simple formulas for thermophysical properties of liquid water for heat transfer calculations (from 0 C to 150 C). *Heat. Transf.* **19**, 87–101 (1998).
64. Vargaftik, N. B., Volkov, B. N. & Voljak, L. D. International tables of the surface tension of water. *J. Phys. Chem. Ref. Data* **12**, 817–820 (1983).
65. Doerr, S. H., Dekker, L. W., Ritsema, C. J., Shakesby, R. A. & Bryant, R. Water repellency of soils: the influence of ambient relative humidity. *Soil Sci. Soc. Am. J.* **66**, 401–405 (2002).
66. Liu, F. et al. Evaporation and dispersion of exhaled droplets in stratified environment. *IOP Conf. Ser. Mater. Sci. Eng*. **609**, 042059 (2019).
67. Huhtamäki, T., Tian, X., Korhonen, J. T. & Ras, R. H. Surface-wetting characterization using contact-angle measurements. *Nat. Protoc.* **13**, 1521–1538 (2018).
68. Extrand, C. W. & Kumagai, Y. An experimental study of contact angle hysteresis. *J. Colloid Interface Sci.* **191**, 378–383 (1997).

69. Bormashenko, E. Wetting of real solid surfaces: new glance on well-known problems. *Colloid Polym. Sci.* **291**, 339–342 (2013).
70. Krainer, S. & Hirn, U. Contact angle measurement on porous substrates: Effect of liquid absorption and drop size. *Colloids Surf. A Physicochem. Eng. Asp.* **619**, 126503 (2021).
71. Wang, J. H., Claesson, P. M., Parker, J. L. & Yasuda, H. Dynamic contact angles and contact angle hysteresis of plasma polymers. *Langmuir* **10**, 3887–3897 (1994).
72. Späth, H. *One Dimensional Spline Interpolation Algorithms* (AK Peters/CRC Press, 1995).
73. Thomas, T. R. Characterization of surface roughness. *Precis. Eng.* **3**, 97–104 (1981).
74. Gadelmawla, E. S., Koura, M. M., Maksoud, T. M., Elewa, I. M. & Soliman, H. H. Roughness parameters. *J. Mater. Process Technol.* **123**, 133–145 (2002).
75. Deltombe, R., Kubiak, K. J. & Bigerelle, M. How to select the most relevant 3D roughness parameters of a surface. *J. Scanning Microsc.* **36**, 150–160 (2014).
76. Owens, D. K. & Wendt, R. C. Estimation of the surface free energy of polymers. *J. Appl. Polym. Sci.* **13**, 1741–1747 (1969).
77. Rulison, C. Two-component surface energy characterization as a predictor of wettability and dispersability. *KRUSS Application note AN213*, pp. 1–22 (2000).
78. Polavaram, K. C. & Garg, N. High-fidelity and high-resolution phase mapping of granites via confocal Raman imaging. *Sci. Rep.* **11**, 1–10 (2021).
79. Polavaram, K. C. & Garg, N. Enabling phase quantification of anhydrous cements via Raman imaging. *Cem. Concr. Res.* **150**, 106592 (2021).

ACKNOWLEDGEMENTS

The authors acknowledge the Department of Civil and Environmental Engineering at the University of Illinois at Urbana-Champaign for supporting this work. Also, the contact angle measurements were carried out in part in the Materials Research Laboratory Central Research Facilities, University of Illinois.

AUTHOR CONTRIBUTIONS

H.K. and N.G. designed the experiments. H.K. conducted the experiments. H.K. and N.G. analyzed the data, prepared the figures, and wrote the manuscript. N.G. acquired funding and supervised the study.

COMPETING INTERESTS

The authors declare no competing interests.

ADDITIONAL INFORMATION

Supplementary information The online version contains supplementary material available at https://doi.org/10.1038/s41529-023-00371-4.

Correspondence and requests for materials should be addressed to Nishant Garg.

Reprints and permission information is available at http://www.nature.com/reprints

Publisher's note Springer Nature remains neutral with regard to jurisdictional claims in published maps and institutional affiliations.

Open Access This article is licensed under a Creative Commons Attribution 4.0 International License, which permits use, sharing, adaptation, distribution and reproduction in any medium or format, as long as you give appropriate credit to the original author(s) and the source, provide a link to the Creative Commons license, and indicate if changes were made. The images or other third party material in this article are included in the article's Creative Commons license, unless indicated otherwise in a credit line to the material. If material is not included in the article's Creative Commons license and your intended use is not permitted by statutory regulation or exceeds the permitted use, you will need to obtain permission directly from the copyright holder. To view a copy of this license, visit http://creativecommons.org/licenses/by/4.0/.

© The Author(s) 2023